

Effects of Stress Ratio and Microstructure on Fatigue Failure Behavior of Polycrystalline Nickel Superalloy

H. Zhang , Z.W. Guan, Q.Y. Wang, Y.J. Liu, and J.K. Li

(Submitted August 20, 2017; in revised form January 29, 2018; published online April 12, 2018)

The effects of microstructure and stress ratio on high cycle fatigue of nickel superalloy Nimonic 80A were investigated. The stress ratios of 0.1, 0.5 and 0.8 were chosen to perform fatigue tests in a frequency of 110 Hz. Cleavage failure was observed, and three competing failure crack initiation modes were discovered by a scanning electron microscope, which were classified as surface without facets, surface with facets and subsurface with facets. With increasing the stress ratio from 0.1 to 0.8, the occurrence probability of surface and subsurface with facets also increased and reached the maximum value at $R = 0.5$, meanwhile the probability of surface initiation without facets decreased. The effect of microstructure on the fatigue fracture behavior at different stress ratios was also observed and discussed. Based on the Goodman diagram, it was concluded that the fatigue strength of 50% probability of failure at $R = 0.1, 0.5$ and 0.8 is lower than the modified Goodman line.

Keywords Crack initiation, Goodman diagram, High cycle fatigue (HCF), Nimonic 80A, Stress ratio

1. Introduction

Polycrystalline nickel superalloys are used extensively in a wide range of environments and applications, such as hot sections of gas turbines in the aerospace and power generation industries due to their excellent strength and high oxidation resistance at the service temperature. The fatigue behavior of nickel superalloy during the service has been increasingly focused in recent years. Jiashi Miao et al. (Ref 1) investigated the high cycle fatigue behavior of nickel alloy Rene 88 DT at room temperature with the stress ratio $R = -1$. They proposed that the crack initiation transition to small crack growth was influenced by the twin boundaries and misorientation. Larrouy and Cormier (Ref 2) studied the plasticity and damage processes initiated near grain boundaries and identified the microvolumes at the grain boundary as the crack initiation location. The fatigue strength of nickel superalloy could be determined by microstructures of the alloy and the external work environment such as temperature. However, high cycle fatigue (HCF) was determined as a key cause of numerous

failures in USAF fighter engines (Ref 3, 4). Generally, the “Goodman” diagram, a powerful material design tool and a plot of mean stress and stress amplitude, was employed to obtain the fatigue properties (Ref 5).

As well known, there are many factors which can affect the fatigue crack initiation, propagation and fracture behavior, such as environment (Ref 6-9), microstructure (Ref 10-14) and stress ratio (Ref 15-18). Stephen D. Antolovich (Ref 19) reviewed microstructural, deformation mode, environment and cycle time of fatigue in nickel superalloys. Jiashi Miao et al. (Ref 1, 20) systematically investigated the HCF and very high cycle fatigue behavior of Rene 88DT from the perspective of microstructures. Guolei Miao et al. (Ref 21) performed high cycle and very high cycle fatigue of FGH96 at 600 °C with the $R = 0.05$. Three types of competing failure modes were observed. Findley and Saxena (Ref 22) investigated the low cycle fatigue behavior of Rene 88DT and observed two types of competing failure modes which are sensitive to the grain size. Based on the competing failure behavior induced by the microstructure and stress ratio, a new statistical paradigm of fatigue variability modes was presented by the Jha et al. (Ref 23, 24). They showed that the competing behavior induced by the mean stress and microstructure could provide accurate fatigue response by the new paradigm.

In this paper, Nimonic 80A was chosen to investigate the effects of microstructure and stress ratio on the HCF behavior. The stress ratios of 0.1, 0.5 and 0.8 were selected to perform the high cycle fatigue under a frequency of 110 Hz. The $S-N$ curves were plotted in terms of the stress amplitude and maximum stress, respectively. All the fatigue fracture surfaces were observed using scanning electron microscope (SEM), while three failure types of crack initiation were observed under different stress ratios. The statistical methods, including probability of failure (POF) and lognormal cumulative distribution function (CDF), were used, respectively, to analyze the competition of the failure types corresponding to a specified stress ratio. The Goodman diagram was plotted to gain a better understanding of the effect of stress ratio on fatigue behavior. In addition, the microstructure of fracture surface related to the stress ratio was presented and discussed.

H. Zhang, Failure Mechanics and Engineering Disaster Prevention and Mitigation Key Laboratory of Sichuan Province, College of Architecture and Environment, Sichuan University, Chengdu 610065, China; and Key Laboratory of Deep Underground Science and Engineering, Ministry of Education, College of Architecture and Environment, Sichuan University, Chengdu 610065, China; **Z.W. Guan**, School of Mechanical Engineering, Chengdu University, Chengdu 610106, China; **Q.Y. Wang** and **Y.J. Liu**, Failure Mechanics and Engineering Disaster Prevention and Mitigation Key Laboratory of Sichuan Province, College of Architecture and Environment, Sichuan University, Chengdu 610065, China; and **J.K. Li**, Key Laboratory of Deep Underground Science and Engineering, Ministry of Education, College of Architecture and Environment, Sichuan University, Chengdu 610065, China. Contact e-mails: h.zhang@foxmail.com and wangqy@scu.edu.cn.

2. Materials and Experimental Procedure

2.1 Material Microstructural Characterization

The material used in the study is polycrystalline nickel-based superalloy, Nimonic 80A. The nominal alloy chemical composition is: 0.05% C, 20% Cr, 1.6% Al, 2.5% Ti, Ni (balance) (mass percent). The received material was processed by the forge and aging heat treatments, i.e., 1080 °C/8 h/AC + 850 °C/24 h/AC + 700 °C/16 h/AC (AC: air cooling). The electron backscattering diffraction (EBSD, Oxford Instruments) was employed to analyze the microstructure characters, as shown in Fig. 1 which the alloy has a poor texture. The grain boundary (GB) map is given in Fig. 1(b), where the red lines represent $\Sigma 3$ twin boundaries. The fraction of $\Sigma 3$ twin boundaries is about 55% in the alloy. The average grain size is about 100 μm . The ultimate tensile strength (UTS) and the 0.2% yield strength at room temperature (RT) were about 1223.5 and 797.8 MPa, respectively. A Vickers hardness test (FLC-50VX) was performed to obtain the hardness at RT with 100 g load applied for 15 s. The test path was the cross section of the gauge segment, and test spacing was approximately 100 μm . Finally, the average hardness value of Nimonic 80A was obtained as 366 HV.

2.2 Fatigue Experimental Procedure

Fatigue tests were performed at RT and laboratory air condition in the high cycle fatigue regime using the push-pull high frequency fatigue test equipment (QBG-100) based on ISO 1099:2006 fatigue test standard (Ref 25). The frequency of 110 Hz and stress ratios (R) of 0.1, 0.5 and 0.8 were applied. Cylindrical specimens with a gauge diameter of 4.5 mm and a gauge length of 27.69 mm showed in Fig. 2 were used in the test. Prior tests, all specimens were mirror polished along the gauge length. After fatigue tests, fatigue fracture surfaces of tested specimens were examined using SEM to define the different regions including crack initiation, crack propagation and finally fracture regions.

3. Results and Discussion

3.1 S-N Curves and Fatigue Fracture Surfaces Fractography

Figure 3 shows the S-N curves of nickel superalloy Nimonic 80A with the specified stress ratios of 0.1, 0.5 and 0.8, expressed in the stress amplitude and maximum stress. The red, green and blue lines are the fitted curves with 50% probability of failure at the above stress ratios, respectively. Obviously, all six curves show continuously declining patterns. It is noted that with increase in the stress ratio, the fatigue limit in terms of stress amplitude (σ_a) decreases (Fig. 3a), and the fatigue limit in terms of maximum stress (σ_{max}) increases (Fig. 3b), respectively. Moreover, fatigue lifetime decreases with the increase in the stress ratio at a given stress amplitude. The trend of the stress amplitude and the maximum stress at different stress ratios versus fatigue lifetime is reversed. The fatigue strength represented by the maximum stress is about 840 MPa ($R = 0.8$), which is larger than the yield strength of alloy, and the fatigue strength increases with increase in stress ratio, as shown in Fig. 3(b). Obviously, the tensile mean stress induced microcrack open; on the other hand, the microcrack tip

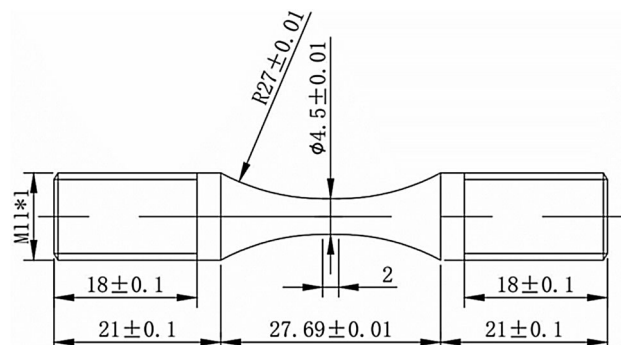


Fig. 2 Schematic of HCF specimen (in mm)

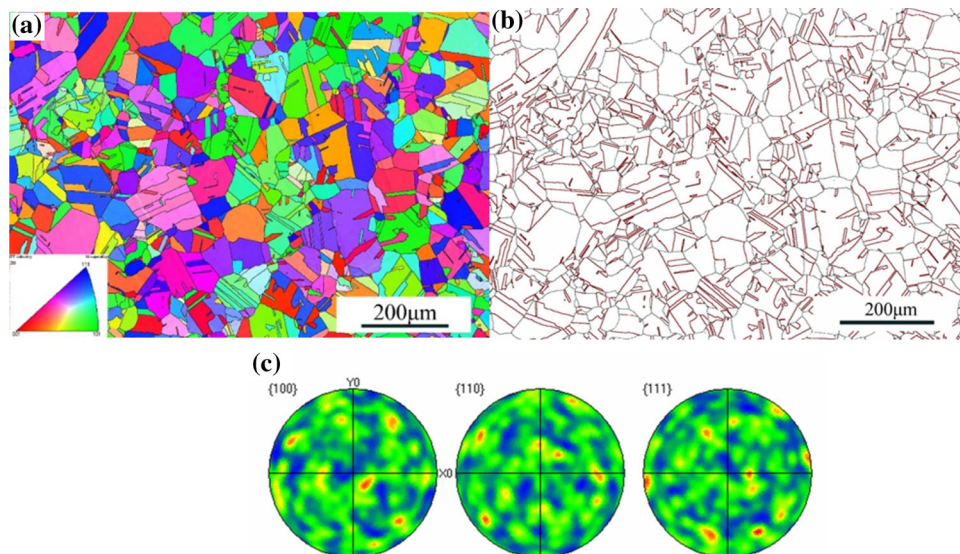


Fig. 1 EBSD characterization of grain microstructure. (a) inverse pole figure map; (b) grain boundary map; (c) pole figure map

will close if there is the plasticity distributed in the crack initiation region.

Based on SEM observations of the fracture surfaces, there are three failure types of the crack initiation mode. Figures 4, 5, and 6 show the details of such three failure types, respectively, i.e., surface without facets, surface with facets and subsurface with facets. The similar phenomenon reports were observed by Liu et al. (Ref 16, 26) with Ti alloy and Miao et al. (Ref 21)

with nickel superalloy. The enlargement of crack initiation region is shown on the right of each SEM image.

Figure 4 displays the fracture morphology of the crack initiation originated from the surface without facets, which is named as “surface without facets” for failure type I. Liu et al. (Ref 16) studied the effect of stress ratios on high cycle fatigue behavior of Ti alloy. They also observed the same failure type. Figure 4(c) gives the schematic of type I. As it is shown, the

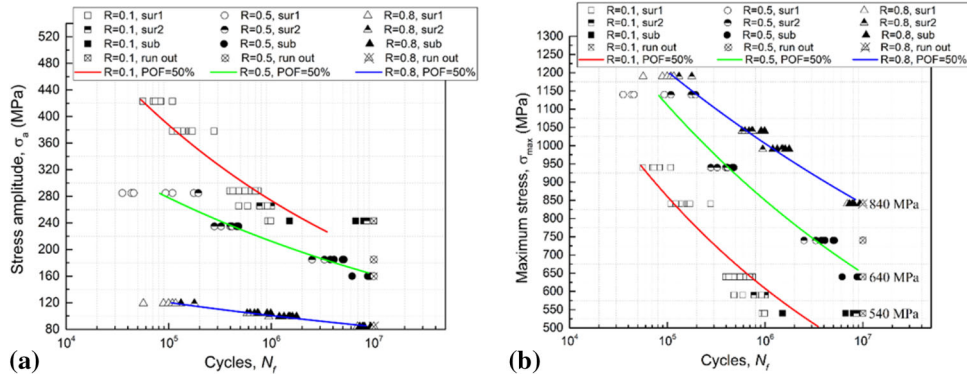


Fig. 3 S–N curves of the Nimonic 80A alloy with stress ratio of 0.1, 0.5 and 0.8. (a) stress amplitude, σ_a vs. N_f , (b) maximum stress, σ_{max} vs. N_f (sur1: surface without facets; sur2: surface with facets; sub: subsurface with facets)

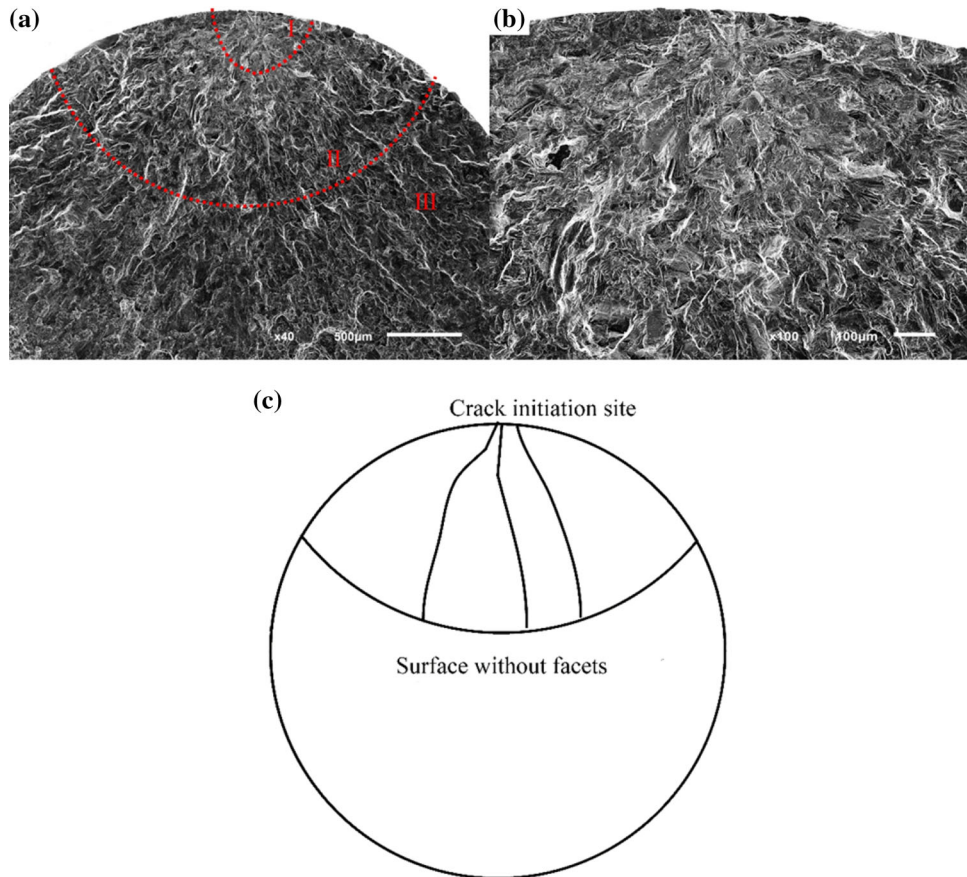


Fig. 4 Typical failure type of surface without facets, $R = 0.1$, $\sigma_{max} = 940$ MPa, $N_f = 8.4 \times 10^4$. (a) low magnification; (b) enlargement of initiation region; (c) schematic of failure type I

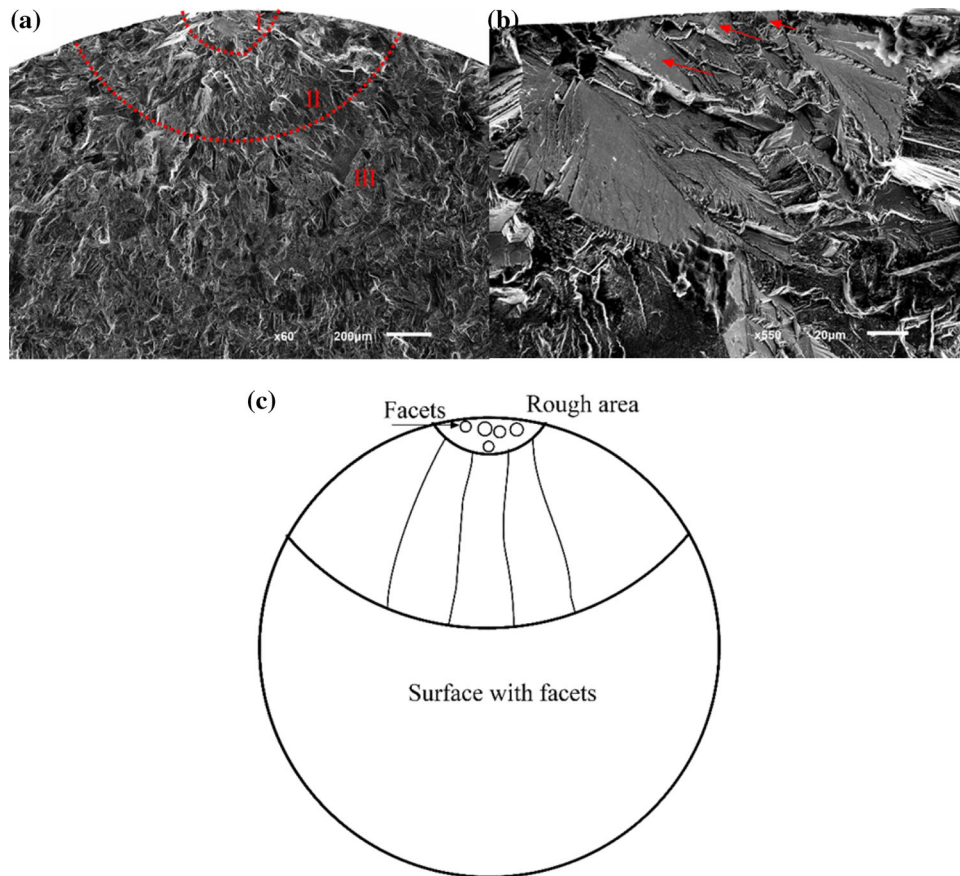


Fig. 5 Typical failure type of surface with facets, $R = 0.5$, $\sigma_{\max} = 740$ MPa, $N_f = 3.305 \times 10^6$. (a) low magnification; (b) enlargement of initiation region; (c) schematic of failure type II

entire fracture surface can be divided into three typical regions by the red dashed lines. The region I covers the smooth area which is the crack initiation site; the region II is a rough area without facets with many river-like ridges along the crack propagation direction; the region III is comparatively flat with fatigue stripes along the crack growth direction. Thus, the region II and III need to be defined in the crack propagation regions (Ref 27).

The failure morphology of failure type II is presented in Fig. 5, in which the crack initiation was developed from the surface with facets randomly distributed at the initiation site, as shown in Fig. 5(a) that is cleavage facets failure and named “surface with facets.” The similar failure type was observed in nickel alloy by Miao et al. (Ref 21). Figure 5 (c) shows the schematic of type I, which can also be divided into three regions the same as discussed of type II. The facets are the cleavage failure type located in the surface area which indicates that the crack initiates from the cleavage and propagate along the cleavage (Ref 28).

Type III is named as “subsurface with facets” which means crack initiation arises from the subsurface with many facets randomly distributed in the initiation region, as shown in Fig. 6(a), with the similar phenomenon reports by Liu et al. (Ref 16, 26) and Jiashi Miao et al. (Ref 20). Again, the fracture

surface can also be split into three regions including crack initiation rough area (region I), crack propagation regions (region II and III). Figure 6(c) shows the schematic of failure type III. As the stress ratio increases, the facet area expands, and the density of facets clearly increases.

Based on the fracture morphology observation, the occurrence probability of failure type is plotted as a function of the stress ratio, as shown in Fig. 7, where the occurrence probability of surface and subsurface with facets is first increased with the increasing stress ratio, and reaches the maximum value at $R = 0.5$, then, surface with facets minor declines and subsurface with facets slowly increases until $R = 0.8$. The trend of surface without facets quickly declines from $R = 0.1$ to 0.5, after that the decline becomes minor. Thus, it can be seen that the $R = 0.5$ is a key point, with which the same trend is also observed in Fig. 3. However, it is well known that the increasing stress ratio leads to increase in the maximum stress and results in the restraint of surface initiation and activation of the subsurface initiation (Ref 16). This is in accordance with the experimental observations.

Figure 8 shows the lognormal cumulative distribution function (CDF) at different stress ratios, in which the experimental data are dealt with the lognormal probability space based on the linearization of the CDF (Ref 23, 24, 29). From

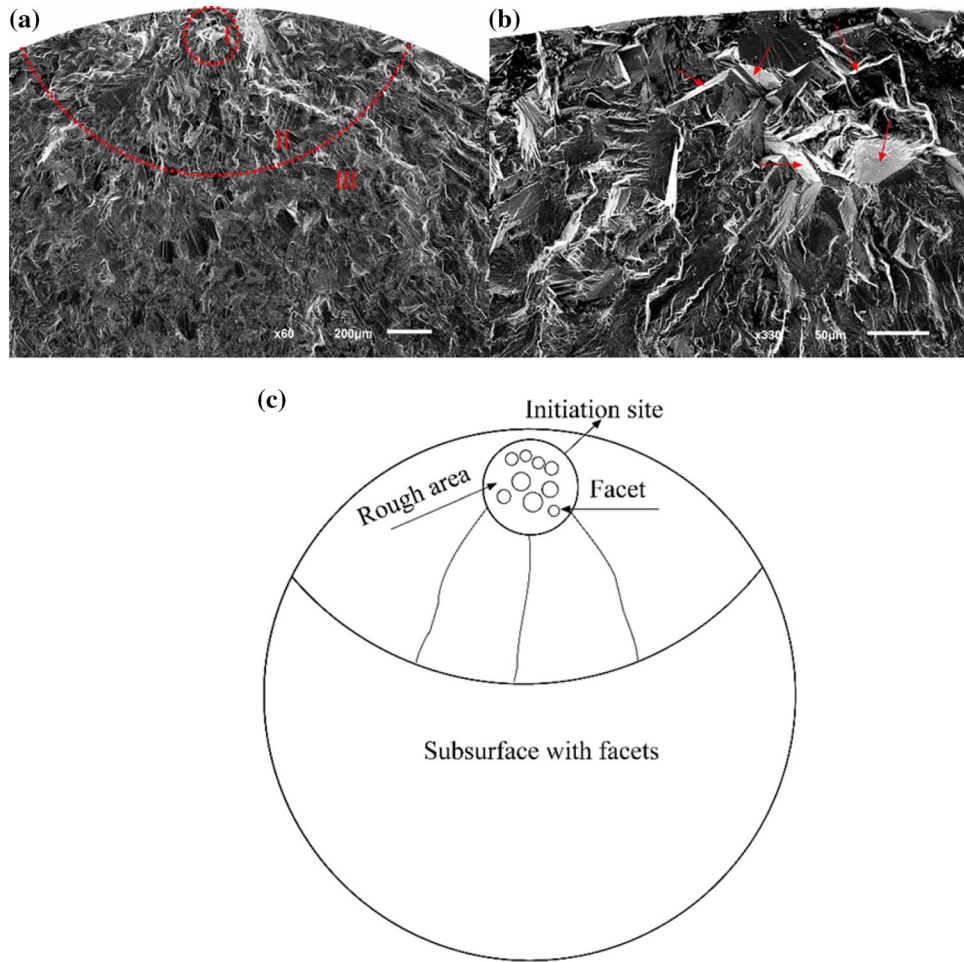


Fig. 6 Typical failure type of subsurface with facets, $R = 0.8$, $\sigma_{\max} = 990$ MPa, $N_f = 1.7664 \times 10^6$. (a) low magnification; (b) enlargement of initiation region; (g) schematic of failure type III

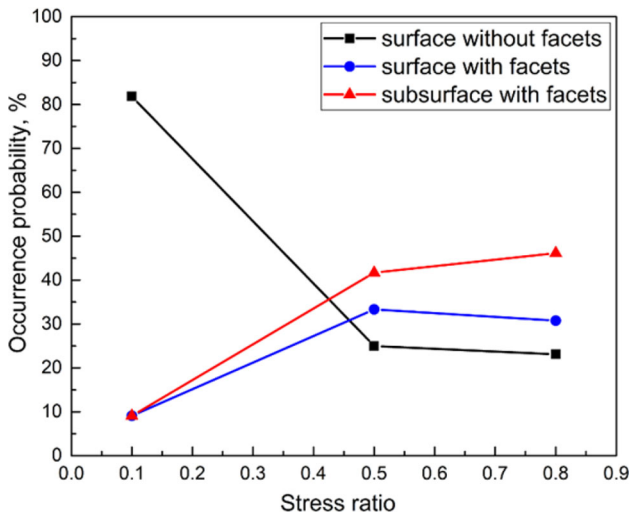


Fig. 7 Occurrence probability of failure types with a function of the stress ratio

Fig. 8(a), it is noted that the trend of the fitted curves, except for the black fitted curve, is similar at $R = 0.1$. However, at the lowest stress level of $\sigma_a = 243$ MPa, the experimental data present a step-like shape with the CDF response. This step-like shape of the CDF was reported previously (Ref 15, 30, 31). It is well known that such the shape developed from the superposition of two failure mechanisms at the same stress level and described in the function by Jha et al. (Ref 29, 30), in which one is dominated by crack growth (lower life failures), and another is controlled by the crack initiation (higher life failures) due to the effect of the mean stress. For RT fatigue tests, there are three failure types, i.e., surface without facets, surface with facets and subsurface with facets, as shown in Fig. 4, 5 and 6. In addition to that, there is no exact source of crack initiation in a SEM. Thus, the competing mechanisms of step-like shape is surface (lower parts of shape) and subsurface (upper parts of shape) crack initiation failure, respectively. In Fig. 8(b), all the experimental points are fitted in a linear fashion with variable slopes at $R = 0.5$. However, the slopes of the CDF lines with increase in the mean stress at $R = 0.8$ have little change, as

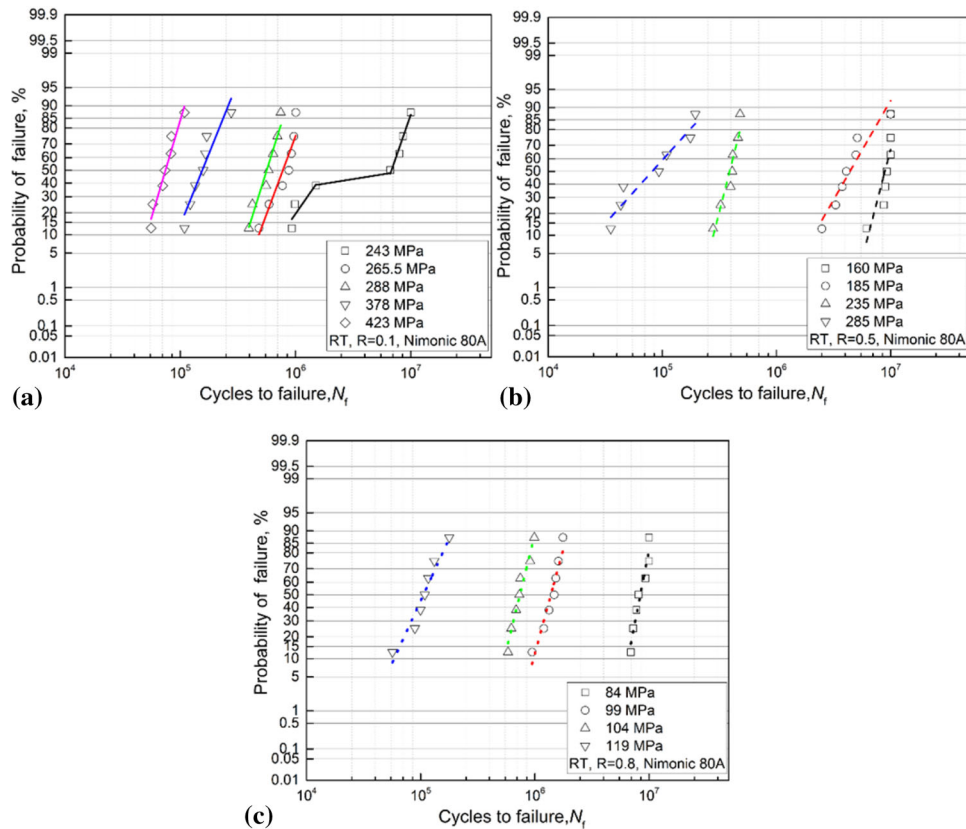


Fig. 8 Probability of failure plots with stress amplitude at different stress ratios. (a) CDF plots at $R = 0.1$; (b) CDF plots at $R = 0.5$; (c) CDF plots at $R = 0.8$

shown in Fig. 8(c), with the similar phenomenon reported by Tanaka and Laz (Ref 32, 33).

Figure 9 shows that the life limit behavior (the minimum, mean and 0.1% POF lifetime) is the function of the stress level with stress ratios of 0.1, 0.5 and 0.8. It is well known that the 0.1% POF lifetime is the most conservative and most important design parameters during fatigue regime. All the minimum, mean and 0.1% POF lifetime decreases as stress level increases, but with different responses. Jha et al. (Ref 23, 24) studied the fatigue variability behavior of titanium alloy with this method and had similar results. They believed that it is evidence of the existence of different competitive failure mechanism. All the mean life is larger than the minimum and 0.1% POF life at $R = 0.1, 0.5$ and 0.8 . Clearly, 0.1% POF life is the biggest at $\sigma_a = 243$ MPa in Fig. 9(a) due to the lowest stress level. This indicates that the mean, minimum and 0.1% POF life behavior should be governed by different mechanisms (Ref 24), same as that discussed in Fig. 8. With increasing the stress level, the difference is gradually declined. The distribution trend of $R = 0.5$ and 0.8 is similar. However, with increase in the stress ratio, the fatigue strength decreases. As shown in Fig. 9, another consequence of the response is that 0.1% POF lifetime decreases with increase in the stress amplitude under every

stress ratios (0.1, 0.5 and 0.8). And with increase in the stress ratio, the stress amplitude decreases and the mean stress increases, which induced the microcrack open and result in fatigue strength decreases. This is in agreement with the experimental results in Fig. 3(a).

3.2 The Effect of Stress Ratio on Fractographic Feature of Fatigue Fracture Behavior

Based on the SEM observation of the failure surfaces, this work attempts to estimate the influence of stress ratios on the fractographic feature of fatigue fracture behavior. Typical fracture surface was selected at each stress ratio including crack initiation, propagation and finally fracture regions, respectively.

Figure 10 presents the fatigue fractographic fracture surface at $R = 0.1$ with the maximum stress of 590 MPa and lifetime of 1.0081×10^6 . The overall fracture surface reveals the distinct regions of fatigue (crack initiation and propagation) and overload (final fracture region), as shown in Fig. 10(a), in which the initiation region is almost at 90° to the far-field stress direction. The highly magnified observation in Fig. 10(b) presents the crack initiation with facets (region I) and radial river-like ridges along the crack propagation direction

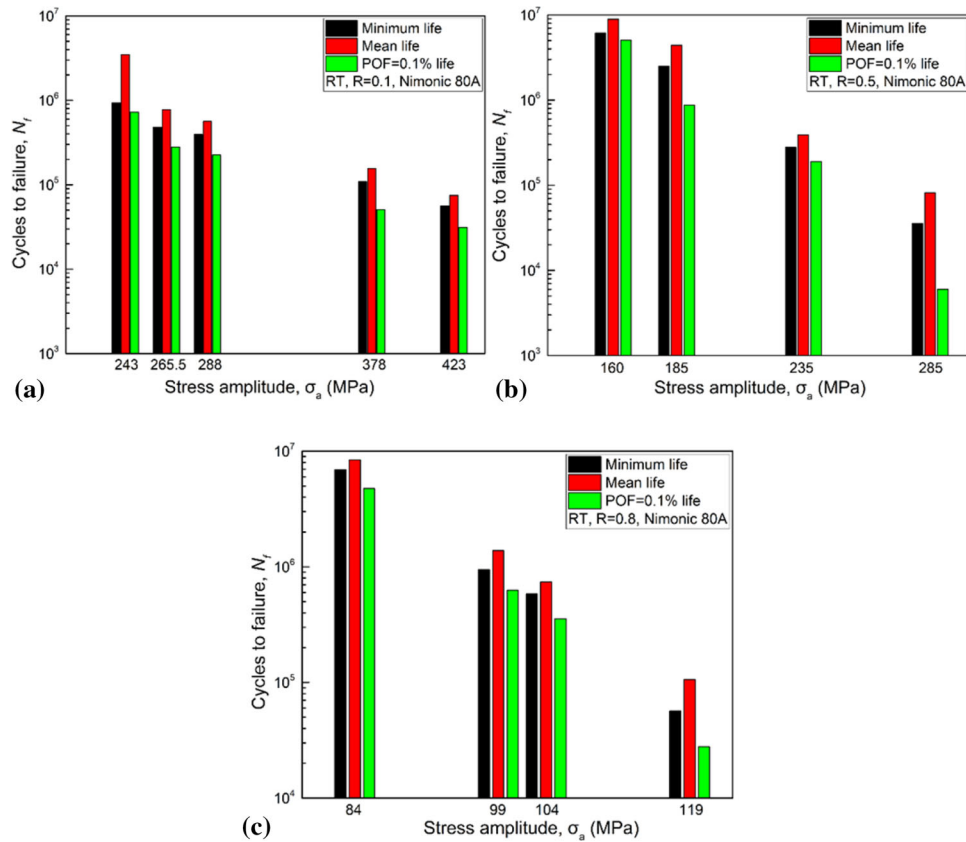


Fig. 9 Comparison of the 0.1% POF lifetime with the mean and minimum lifetime of Nimonic 80A at different stress ratios. (a) $R = 0.1$; (b) $R = 0.5$; (c) $R = 0.8$

(region II). The region of stable crack growth with about 1.579 mm from the crack initiation region displayed in Fig. 10(a) shows the fine and orderly fatigue striations and radial river-like streaks along the crack propagation direction mixed with some random striations, as shown in Fig. 10(c). Ductile dimples and some deformation caused by brittle fracture are also observed at the final fracture region, as shown in Fig. 10(d). This indicates that the failure mechanism is dominated by the locally ductile microplasticity and brittle fracture (Ref 27).

Figure 11 displays the fracture surface at $R = 0.5$ with the maximum stress of 740 MPa and number of cycles to the failure 3.305×10^6 . The crack initiation and early propagation regions are flat and featureless in Fig. 11(a), where the failure mechanism is controlled by transgranular fracture. With a high magnification, Fig. 11(b) reveals the radial river-like ridges along the crack propagations direction. A high-magnification observation of the stable crack growth region which is about 1.365 mm from the crack initiation region reveals clearly that the striations and microscopic cracks are randomly distributed, as shown in Fig. 11(c). Ductile dimples and a few deformations caused by brittle fracture present in the final fracture region are shown in Fig. 11(d). These features also present an evidence of

the principal ductile and isolated brittle fracture mechanisms at the final fracture region.

Figure 12 shows SEM images of the fracture surface related to the stress ratio (i.e., $R = 0.8$) with a maximum stress of 990 MPa and fatigue failure cycles of 1.7664×10^6 . It is visible that the crack initiation region is different from the other regions in the overall fracture surface, as shown in Fig. 12(a). Careful high-magnification observation of the initiation and propagation regions, Fig. 12(b) reveals the cleavage facet and intergranular fracture. Very small and randomly distributed striations are also presented in this region. The final fracture region is covered with dimples and deformation caused by brittle fracture, as shown in Fig. 12(c). This is attributed to the occurrence of both ductile and brittle failure mechanisms.

The aim of this study is attempted to assess and establish the influence of stress ratio on fatigue properties and fractographic feature. There are many dimples found covering the final fracture surface, which indicates the “locally” ductile failure (Ref 34, 35). The crack propagation region becomes small and the final fracture region size increases with increasing the stress ratio. With increase in stress ratio, the maximum stress increases, and the mean stress also increases, which results in

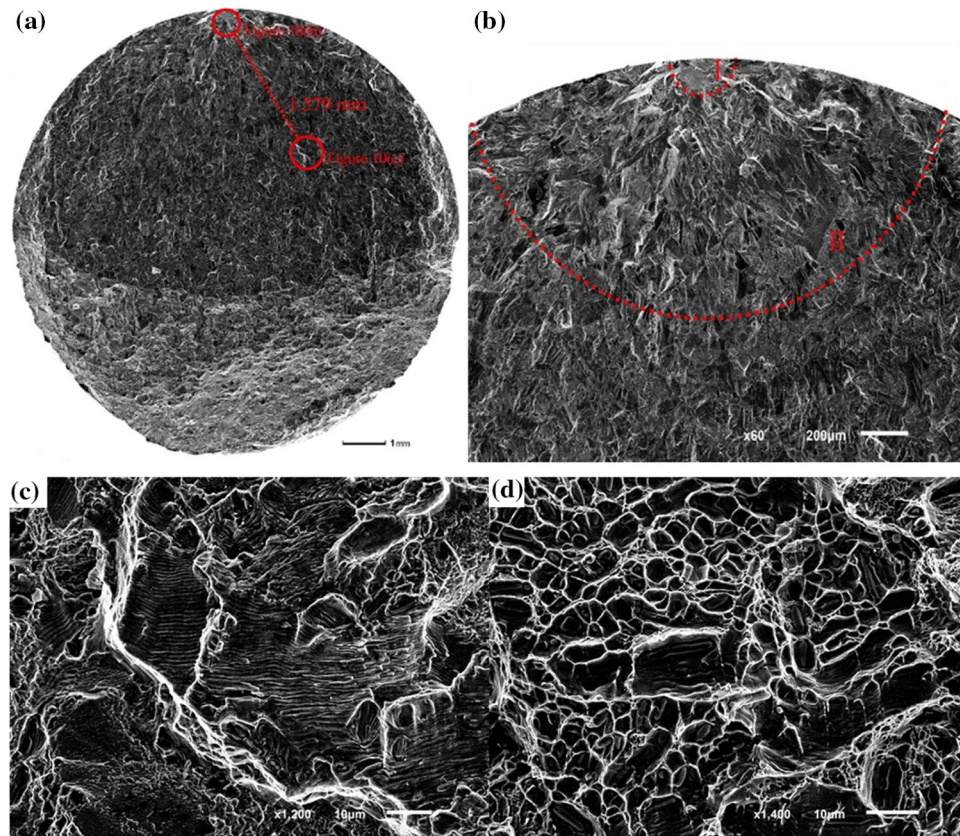


Fig. 10 SEM observations at $R = 0.1$, $\sigma_{\max} = 590$ MPa, $N_f = 1.0081 \times 10^6$. (a) Overall fracture surface; (b) high magnification of crack initiation and propagation region; (c) high magnification of stable crack growth with striations; (d) the final fracture region

the suppression of surface crack initiation and activation of the subsurface crack initiation with facets, in other words, maximum stress controls the cleavage failure, the stress amplitude dominates the slip deformation, as shown in Fig. 3, 4, 5, 6 and 7. And at low cyclic stress and enhanced lifetime with three stress ratios, crack initiation originates from twin boundaries (Ref 36) and the density of slip decreases with decreasing the cyclic stress (Ref 37) which is in agreement with the experimental results in Fig. 3. This also can explain why crack initiation predominately originates from facets on the surface and in the subsurface area at 10^6 - 10^7 cycles. At high cyclic stress and resultant low lifetime with stress ratio of 0.1, 0.5 and 0.8, plastic deformation takes place in all surface grains. Then, deformation incompatibility of adjacent grains is appeared due to the different misorientations of each grain (Ref 38). Thus, stress concentration at grain boundaries is presented which is the crack initiation sites in the low cycle fatigue regime.

3.3 The Effects of Mean Stress on Fatigue Strength

Figure 13 presents the relationship between stress amplitude (σ_a) and mean stress (σ_m) based on the Goodman diagram

approach. This is the useful tool for investigating the effect of mean stress on the fatigue strength. The red solid line is the modified Goodman approximation, which gives a linear relationship between the fatigue limit at $R = -1$ and the ultimate tensile strength. The modified Goodman is usually treated as conservative results because of the high safety margin for designing and engineering purpose.

All the fatigue strength obtained for $R = 0.1$, 0.5 and 0.8 are lower than the modified Goodman line. However, the results of $R = 0.1$ are closer to the Goodman line than others. The failure behavior of $R = 0.1$ is mainly controlled by surface initiation. With increase in the stress ratio, the maximum stress increases and the mean stress increases, and the failure behavior transforms from surface initiation to mixed with surface and subsurface initiation which crack was revealed at a vacuum-like environment and fatigue crack growth rate was lower in vacuum than in air (Ref 6, 39). Also, at given stress amplitude, with increase in stress ratio, the mean stress increases and result in the crack initiated from surface to subsurface. In order words, the surface and subsurface initiation can be retrained and active, respectively, at a high stress ratio or high mean stress. As shown in Fig. 13, the high stress ratios (0.5 and 0.8) have lower than low stress ratio (0.1) because the subsurface crack

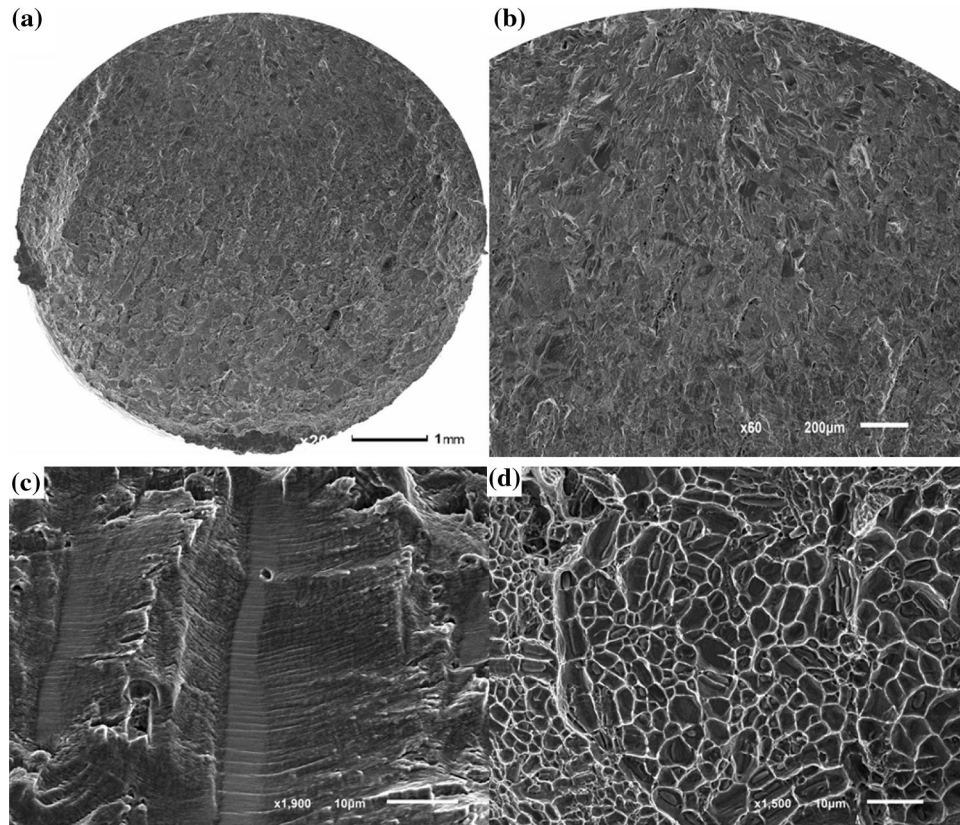


Fig. 11 SEM observations at $R = 0.5$, $\sigma_{\max} = 740$ MPa, $N_f = 3.305 \times 10^6$. (a) Overall fracture surface; (b) high magnification of crack initiation and propagation region; (c) high magnification of stable crack growth with striations; (d) the final fracture region

initiation needs much more time than surface crack initiation at same mean stress.

4. Conclusions

1. For stress ratios of 0.1, 0.5 and 0.8, the $S-N$ curves based on the stress amplitude and maximum stress show a continuous decline trend. With increase in the stress ratio, the fatigue limit expressed in stress amplitude decreases and maximum stress increases.
2. Three crack initiation failure types are observed and grouped into the surface without facets, surface with facets and subsurface with facets. The occurrence probability of failure types is defined with a function of the stress

- ratio. With increase in the stress ratio, the occurrence of surface with facets and subsurface with facets increases first and then gradually declines and that for surface without facets continuously decreases.
3. Evaluation of microstructure of fatigue crack initiation, propagation and fracture locations at stress ratios of 0.1, 0.5 and 0.8 shows that transgranular and intergranular fracture dominates the crack initiation and early crack propagation. With increase in the stress ratio, the maximum stress and mean stress increases, and result in the failure mechanism transforms from surface to subsurface, while the crack propagation region decreases and the final fracture region gradually increases.
4. The high cycle fatigue limit obtained for $R = 0.1$, 0.5 and 0.8 is lower than the modified Goodman line. And

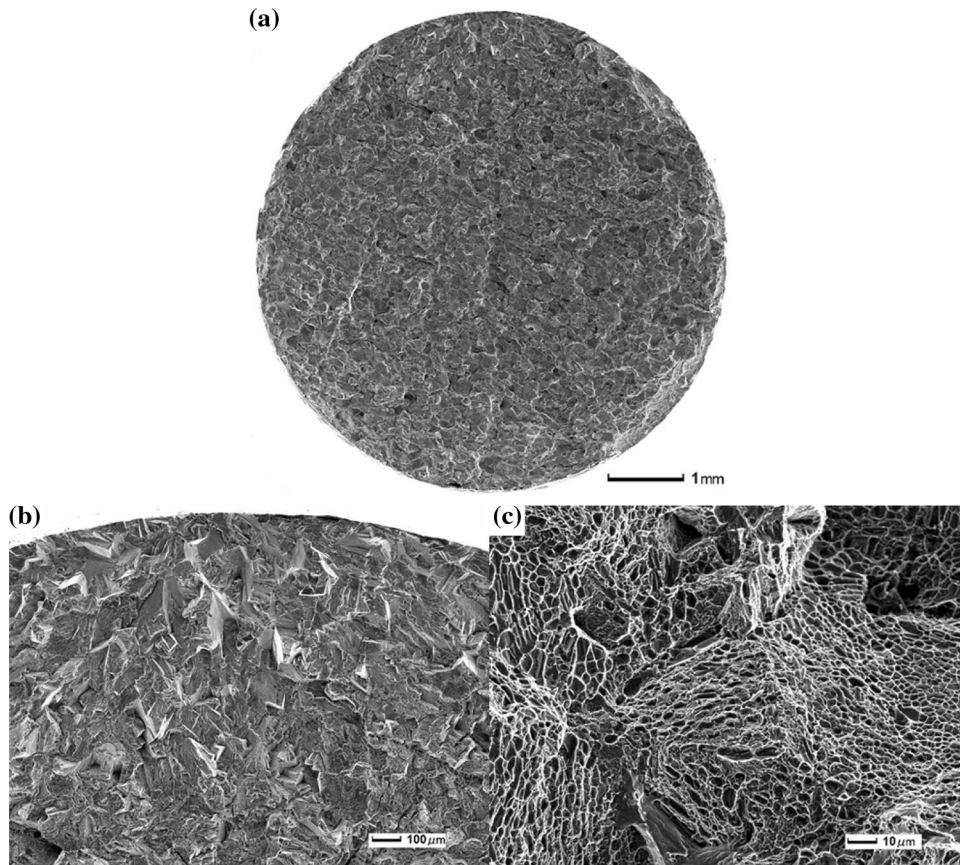


Fig. 12 SEM observations at $R = 0.8$, $\sigma_{\max} = 990$ MPa, $N_f = 1.7664 \times 10^6$. (a) Overall fracture surface; (b) high magnification of crack initiation and propagation region; (c) the final fracture region

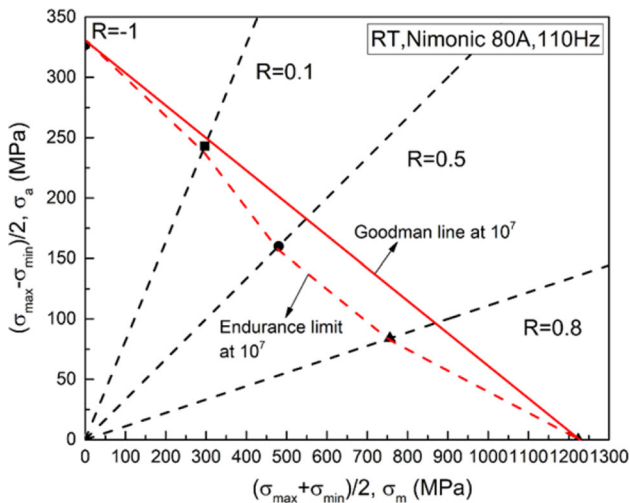


Fig. 13 Goodman diagram approach to estimate the fatigue strength at various R

the high stress ratio can retrain the surface initiation and activate the subsurface fatigue crack initiation. Mean stress has a very obviously influence on the fatigue strength of this alloy as evidenced by the shape of the Goodman diagram, which must be considered in damage tolerant design for HCF.

Acknowledgments

This work was supported by the National Natural Science Research Foundation of China (Nos. 11327801, 11502151, 11572057), the Program for Changjiang Scholars and Innovative Research Team (No. IRT14R37), and Key Science and Technology Support Program of Sichuan Province (No. 2015JPT0001).

References

1. J. Miao, T.M. Pollock, and J. Wayne Jones, Microstructural Extremes and the Transition from Fatigue Crack Initiation to Small Crack Growth in a Polycrystalline Nickel-Base Superalloy, *Acta Mater.*, 2012, **60**(6), p 2840–2854
2. B. Larrouy, P. Villechaise, J. Cormier, and O. Berteaux, Grain Boundary–Slip Bands Interactions: Impact on the Fatigue Crack Initiation in a Polycrystalline Forged Ni-Based Superalloy, *Acta Mater.*, 2015, **99**, p 325–336
3. T. Nicholas and J.R. Zuiker, On the Use of the Goodman Diagram for High Cycle Fatigue Design, *Int. J. Fract.*, 1996, **80**(2–3), p 219–235
4. B.A. Cowles, High Cycle Fatigue in Aircraft Gas Turbines—An Industry Perspective, *Int. J. Fract.*, 1996, **80**(2), p 147–163
5. T. Nicholas, Critical Issues in High Cycle Fatigue, *Int. J. Fatigue*, 1999, **21**(99), p S221–S231
6. H. Oguma and T. Nakamura, Fatigue Crack Propagation Properties of Ti-6Al-4 V in Vacuum Environments, *Int. J. Fatigue*, 2013, **50**, p 89–93
7. Y. Gao, M. Kumar, R.K. Nalla, and R.O. Ritchie, High-Cycle Fatigue of Nickel-Based Superalloy ME3 at Ambient and Elevated Temperatures: Role of Grain-Boundary Engineering, *Metall. Mater. Trans. A*, 2005, **36A**(12), p 3325–3333

8. M.J. Caton and S.K. Jha, Small Fatigue Crack Growth and Failure Mode Transitions in a Ni-Base Superalloy at Elevated Temperature, *Int. J. Fatigue*, 2010, **32**(9), p 1461–1472
9. X. Huang, L. Wang, Y. Hu, G. Guo, D. Salmon, Y. Li, and W. Zhao, Fatigue Crack Propagation Behavior of Ni-Based Superalloys After Overloading at Elevated Temperatures, *Progr. Nat. Sci. Mat. Int.*, 2016, **26**(2), p 197–203
10. K.S. Chan, Roles of Microstructure in Fatigue Crack Initiation, *Int. J. Fatigue*, 2010, **32**(9), p 1428–1447
11. S.R. Yeratapally, M.G. Glavicic, M. Hardy, and M.D. Sangid, Microstructure Based Fatigue Life Prediction Framework for Polycrystalline Nickel-Base Superalloys with Emphasis on the Role Played by Twin Boundaries in Crack Initiation, *Acta Mater.*, 2016, **107**, p 152–167
12. T. Alp and A. Wazzan, The Influence of Microstructure on the Tensile and Fatigue Behavior of SAE 6150 Steel, *J. Mater. Eng. Perform.*, 2002, **11**(4), p 351–359
13. J. Liu, Q. Zhang, Z. Zuo, and Y. Xiong, Effect of Fatigue Behavior on Microstructural Features in a Cast Al-12Si-CuNiMg Alloy Under High Cycle Fatigue Loading, *J. Mater. Eng. Perform.*, 2013, **22**(12), p 3834–3839
14. K. Tamada, T. Kakiuchi, and Y. Uematsu, Crystallographic Analysis of Fatigue Crack Initiation Behavior in Coarse-Grained Magnesium Alloy Under Tension-Tension Loading Cycles, *J. Mater. Eng. Perform.*, 2017, **26**(7), p 3169–3179
15. B. Oberwinkler, Modeling the Fatigue Crack Growth Behavior of Ti-6Al-4 V by Considering Grain Size and Stress Ratio, *Mater. Sci. Eng. A*, 2011, **528**(18), p 5983–5992
16. X. Liu, C. Sun, and Y. Hong, Effects of Stress Ratio on High-Cycle and Very-High-Cycle Fatigue Behavior of a Ti-6Al-4 V Alloy, *Mater. Sci. Eng. A*, 2015, **622**, p 228–235
17. L. Bertini, L. Le Bone, C. Santus, F. Chiesi, and L. Tognarelli, High Load Ratio Fatigue Strength and Mean Stress Evolution of Quenched and Tempered 42CrMo4 Steel, *J. Mater. Eng. Perform.*, 2017, **26**(8), p 3784–3793
18. O. Hatamleh, S. Forth, and A.P. Reynolds, Fatigue Crack Growth of Peened Friction Stir-Welded 7075 Aluminum Alloy under Different Load Ratios, *J. Mater. Eng. Perform.*, 2010, **19**(1), p 99–106
19. S.D. Antolovich, Microstructural Aspects of Fatigue in Ni-Base Superalloys, *Philos. Trans.*, 2015, **373**, p 2038
20. J. Miao, T.M. Pollock, and J. Wayne Jones, Crystallographic Fatigue Crack Initiation in Nickel-Based Superalloy René 88DT at Elevated Temperature, *Acta Mater.*, 2009, **57**(20), p 5964–5974
21. G.L. Miao, X.G. Yang, and D.Q. Shi, Competing Fatigue Failure Behaviors of Ni-Based Superalloy FGH96 at Elevated Temperature, *Mat. Sci. Eng. A Struct.*, 2016, **668**, p 66–72
22. K.O. Findley and A. Saxena, Low Cycle Fatigue in Rene 88DT at 650 °C: Crack Nucleation Mechanisms and Modeling, *Metall. Mat. Trans. A*, 2006, **37**(5), p 1469–1475
23. S.K. Jha, J.M. Larsen, and A.H. Rosenberger, Towards a Physics-Based Description of Fatigue Variability Behavior in Probabilistic Life Prediction, *Eng. Fract. Mech.*, 2009, **76**(5), p 681–694
24. S.K. Jha, M.J. Caton, and J.M. Larsen, A New Paradigm of Fatigue Variability Behavior and Implications for Life Prediction, *Mater. Sci. Eng. A*, 2007, **468–470**, p 23–32
25. Metallic Materials—Fatigue Testing—Axial Force-Controlled Method, ISO 1099:2006, International Organization for Standardization 2006
26. X. Liu, C. Sun, and Y. Hong, Faceted Crack Initiation Characteristics for High-Cycle and Very-High-Cycle Fatigue of a Titanium Alloy Under Different Stress Ratios, *Int. J. Fatigue*, 2016, **92**, p 434–441
27. K. Manigandan, T.S. Srivatsan, T. Quick, S. Sastry, and M.L. Schmidt, Influence of Microstructure and Load Ratio on Cyclic Fatigue and Final Fracture Behavior of Two High Strength Steels, *Mater. Des.*, 2014, **55**, p 727–739
28. A. Pineau, A.A. Benzerga, and T. Pardoen, Failure of Metals I: Brittle and Ductile Fracture, *Acta Mater.*, 2016, **107**, p 424–483
29. S.K. Jha, J.M. Larsen, A.H. Rosenberger, and G.A. Hartman, Dual Fatigue Failure Modes in Ti-6Al-2Sn-4Zr-6Mo and Consequences on Probabilistic Life Prediction, *Scripta Mater.*, 2003, **48**(12), p 1637–1642
30. S.K. Jha, J.M. Larsen, and A.H. Rosenberger, The Role of Competing Mechanisms in the Fatigue Life Variability of a Nearly Fully-Lamellar γ -TiAl Based Alloy, *Acta Mater.*, 2005, **53**(5), p 1293–1304
31. A.H. Fischer, A. Abel, M. Lepper, A.E. Zitzelsberger, and A. von Glasow, Modeling Bimodal Electromigration Failure Distributions, *Microelectron. Reliab.*, 2001, **41**(3), p 445–453
32. S. Tanaka, M. Ichikawa, and S. Akita, A Probabilistic Investigation of Fatigue Life and Cumulative Cycle Ratio, *Eng. Fract. Mech.*, 1984, **20**(3), p 501–513
33. P.J. Laz, B.A. Craig, and B.M. Hillberry, A Probabilistic Total Fatigue Life Model Incorporating Material Inhomogeneities, Stress Level and Fracture Mechanics, *Int. J. Fatigue*, 2001, **23**(1), p 119–127
34. S. Stanzl-Tscheegg and B. Schönbauer, Near-Threshold Fatigue Crack Propagation and Internal Cracks in Steel, *Procedia Eng.*, 2010, **2**(1), p 1547–1555
35. R.H.V. Stone, T.B. Cox, J.R. Low, and J.A. Psioda, Microstructural Aspects of Fracture by Dimpled Rupture, *Int. Metals Rev.*, 2013, **30**(1), p 157–180
36. A. Kolyshkin, M. Zimmermann, E. Kaufmann, and H.-J. Christ, Experimental Investigation and Analytical Description of the Damage Evolution in a Ni-Based Superalloy Beyond 106 Loading Cycles, *Int. J. Fatigue*, 2016, **93**, p 272–280
37. C. Stocker, M. Zimmermann, and H.J. Christ, Localized Cyclic Deformation and Corresponding Dislocation Arrangements of Polycrystalline Ni-Base Superalloys and Pure Nickel in the VHCF Regime, *Int. J. Fatigue*, 2011, **33**(1), p 2–9
38. C. Blochwitz, R. Richter, W. Tirschler, and K. Obtrlik, The Effect of Local Textures on Microcrack Propagation in Fatigued F.C.C. Metals, *Mater. Sci. Eng. A*, 1997, **234**, p 563–566
39. S.E. Stanzl-Tscheegg, O. Plasser, E.K. Tscheegg, and A.K. Vasudevan, Influence of Microstructure and Load Ratio on Fatigue Threshold Behavior in 7075 Aluminum Alloy, *Int. J. Fatigue*, 1999, **21**, p S255–S262